A Multi-operator Approach for the Segmentation of 3-D Images of Dental Imprints.

Jean Côté, Denis Laurendeau and Denis Poussart
Computer Vision & Digital System
Department of Electrical Engineering, Laval University.
Québec, Province of Québec, Canada, G1K 7P4

Abstract

This paper presents a computer vision system for the acquisition and processing of 3-D images of wax dental imprints recorded on human subjects. The system is dedicated to orthodontic diagnosis and epidemiological studies. The acquisition system is described in detail and experimental results are presented. The accuracy of the system is tested on a reference imprint.

A segmentation algorithm is used for the detection of the interstices between teeth on the 3-D images of the imprint. A multi-operator approach is developed in order to be able to deal with teeth of different shape and size. Experiments performed on a large number of imprints show that the algorithm for interstice detection and position estimation is reliable and accurate.

1. Introduction

The detection and correction of development of malocclusions and other dental abnormalities is one of the most important and critical phases of orthodontic diagnosis. The Department of Dentistry and the Computer Vision and Digital Systems Laboratory of Laval University are jointly working on the development of an expert system for orthodontic diagnosis and epidemiological studies. The expert system accepts a set of 10 orthodontic parameters as an input and produces a diagnosis based on inference rules considering the relations between the parameters [2] [3]. The diagnosis consists of one out of three choices: *i)* orthodontic treatment required, *ii)* elective orthodontic treatment, and *iii)* no treatment required. Actually, the orthodontic parameters are measured with great difficulty on costly plaster models. These models are obtained manually by specialized personnel and require a rather complex and lengthy acquisition procedure. A mold of the inside of the mouth must first be obtained. The acquisition of the mold is a very unpleasant experience for the patient. The plaster model is then cast into the mold. The plaster model must be manually improved to remove beards. The team at Laval University is actually working on the design of a computer vision-based 3-D data acquisition and analysis system for the measurement of orthodontic parameters. Instead of using costly plaster models, low-cost wax wafers are used to obtain an imprint of the teeth on both maxillaries.

This paper presents a computer vision system for the acquisition of 3-D profiles of both sides of the imprint recorded on the wax wafer. The acquisition system uses a specially designed 3-D camera based on the differential absorption of light by a dispersive medium. The 3-D profiles are used to detect the interstices between teeth on the maxillaries. The detection of these interstices is a very important step towards automatic measurement of orthodontic parameters. Since incisors, canines, pre-molars, and molars have very different shapes, several operators are combined for the segmentation of the 3-D images and the detection of the interstices.

The paper is divided as follows. Section 2 describes the acquisition setup that was designed for the acquisition of the 3-D profiles of wax dental imprints, and Section 3 presents experimental results of the acquisition of profiles. Accuracy of the 3-D data is also analyzed in this section. Section 4 describes the operators that were designed for the detection of interstices between teeth. Three operators are discussed: the case of upper maxillary incisors, the case of molars on both maxillaries, and the case of lower maxillary incisors. Finally, Section 5 presents experimental results of the segmentation technique for the detection of interstices between teeth and the robustness of the technique is discussed.

2. Acquisition

The dental imprints are first recorded by having the patient bite a low cost wax wafer similar to the one shown in Figure 1. Using these imprints we obtain a three-dimensional

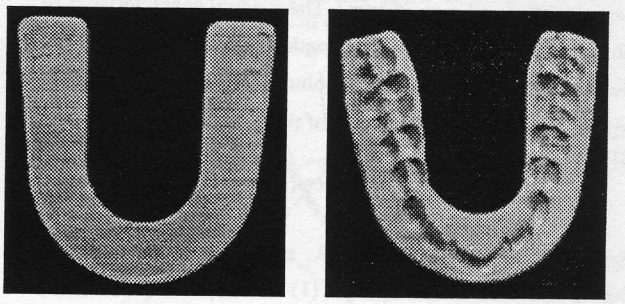

(a) Wafer (b) Wafer with a recorded imprint

Figure 1 Wax wafer.

(3-D) image of both sides of the wafer with a special data acquisition system based on the differential absorption of light by a dispersive medium. The acquisition system is composed of two cameras, two optical bandpass filters of different central wave-lengths, two light sources, and a glass container filled with a colored liquid which acts as a dispersive medium. These components of the system are located on both sides of the container as shown in Figure 2.

The technique that is used to measure the 3D profile (e.g. 3-D image) of the wax wafer is very simple. The wafer is

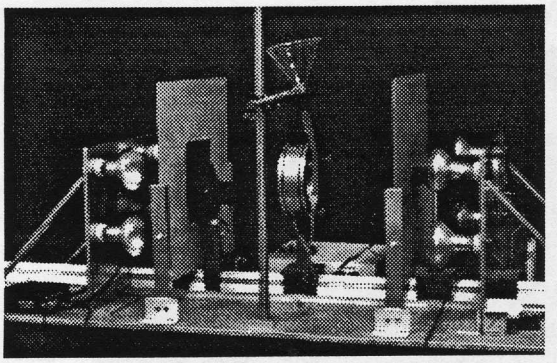

Figure 2 Data acquisition system.

mounted on a support which is immersed in the container filled with colored liquid. The light system on one side of the container is turned on and a first gray-level image of the wafer is acquired at a wave-length λ_1 which is absorbed exponentially as it penetrates the liquid (for the experiments $\lambda_1 = 600nm$). For this first image, the illuminance $dE_{\lambda_1}(i,j)$ at each image point depends on

1) the depth $z(i,j)$ of the point at the surface of the wafer in the liquid and

2) the local orientation $\cos\phi(i,j)$ of the surface at this point relative to the optical axis of the camera:

$$dE_{\lambda_1}(i,j) = K_1 \cos(\phi(i,j))\, e^{-2\alpha z(i,j)} \qquad (1)$$

A second gray-level image of the wafer is taken at wave-length λ_2 ($\lambda_2 = 750nm$). The spectral characteristics of the liquid are such that wave-length λ_2 is not absorbed. The illuminance $dE_{\lambda_2}(i,j)$ at each point in the second image only depends on the local orientation of the surface $\cos\phi(i,j)$, see [8]:

$$dE_{\lambda_2}(i,j) = K_2 \cos(\phi(i,j)) \qquad (2)$$

Figure 3 shows (a) the image at λ_1 and (b) the image at λ_2. Taking the ratio between Eqs. (1) and (2) and solving for $z(i,j)$ we get:

$$z(i,j) = \frac{1}{2\alpha} ln\left[\frac{dE_{\lambda_2}(i,j)}{dE_{\lambda_1}(i,j)}\right] + \frac{1}{2\alpha} ln\left[\frac{K_1}{K_2}\right] \qquad (3)$$

The range image of the second side of the wafer is obtained similarly. The 3-D images on both sides are in perfect registration. Constants K_1, K_2 and α in Eq. (3) are estimated with a proper calibration procedure using a calibration pattern of known dimensions. This pattern is a 13 step staircase. The depth between each step is 1mm. Figure 4 shows the calibration staircase. The ratio $\frac{dE_{\lambda_1}(i,j)}{dE_{\lambda_2}(i,j)}$ is obtained

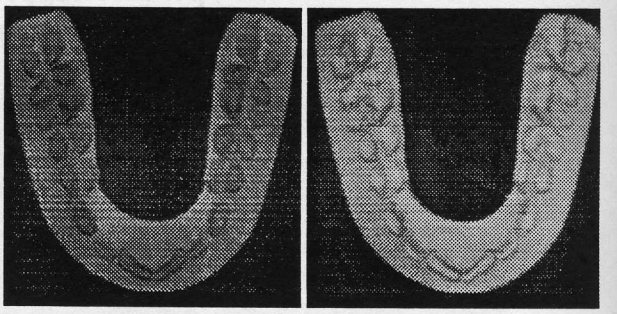

a) λ_1 b) λ_2

Figure 3 Image at λ_1 and λ_2

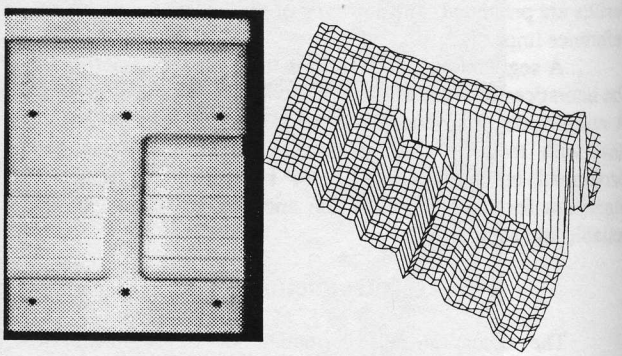

Figure 4 Staircase for calibration.

experimentally for each step S_j of known depth z_{S_j}. The parameters in Eq. (3) are then computed with a least-squares method. Figure 5 shows a calibration curve. Cross symbols correspond to experimental values and the solid line is the regression curve.

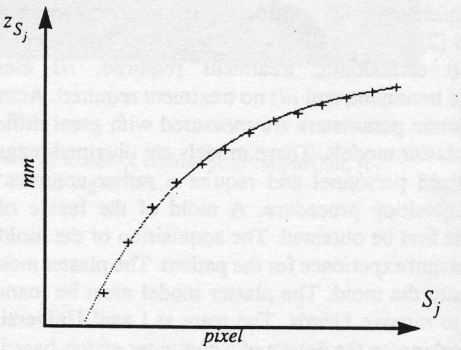

Figure 5 Calibration curve.

3. Validation of 3-D Image Values.

Three-dimensional image data was validated on a machine-made plexiglass model (see Figure 6) similar to an actual wafer. The distance between adjacent teeth, and size and shape of each tooth on the model are known with accuracy. Table 1 compares the values measured with the 3-D acquisition setup on the image of the model to those measured manually on

the model. Lateral measurements on the wafer (not shown in

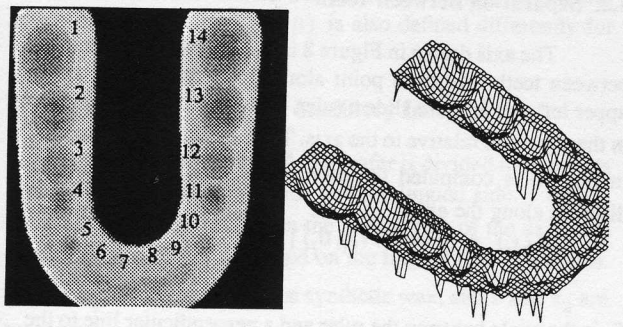

Figure 6 Model for validation.

Table 1) are very accurate (within 5% accuracy). As shown in Table 1 the accuracy on depth measurements is also satisfactory with a relative error ≤ 10%. The error could be decreased by using a better lighting system and by cooling the cameras. The best concentration of the solution for the

	Concentration					
Side 1	0.01%	0.01%	0.02%	0.02%	0.03%	0.03%
1	5.71	1.20	5.71	5.11	5.11	5.11
2	3.97	5.63	2.32	4.97	0.00	3.31
3	7.87	9.45	11.4	2.36	9.44	0.39
4	20.1	20.7	13.1	9.76	19.2	12.5
5	17.0	19.8	9.09	6.32	9.09	9.88
6	7.47	12.1	4.67	7.48	12.1	0.93
7	0.87	5.22	2.61	4.35	9.57	13.0
8	0.93	5.61	7.48	9.35	8.41	1.87
9	2.70	3.60	10.8	6.31	12.6	3.60
10	21.8	22.2	15.6	17.8	8.89	5.78
11	25.6	24.1	6.64	6.64	6.64	3.80
12	0.43	8.70	2.17	4.35	2.17	4.35
13	3.47	2.52	4.10	7.57	7.89	10.4
14	2.07	0.89	5.03	3.55	6.51	5.03

	Concentration					
Side 2	0.01%	0.01%	0.02%	0.02%	0.03%	0.03%
1	6.61	3.58	4.96	3.31	4.68	3.58
2	0.71	1.78	7.14	3.57	6.42	3.57
3	7.69	6.92	1.92	6.92	3.07	7.69
4	17.8	19.2	7.74	14.1	6.40	15.8
5	15.9	13.9	7.56	16.0	4.20	7.56
6	0.00	2.17	6.52	7.61	8.70	0.00
7	4.67	8.41	3.74	7.48	7.48	4.67
8	13.9	0.00	12.0	0.93	15.7	10.2
9	3.36	0.84	6.72	0.00	4.20	0.84
10	24.4	24.4	7.56	11.8	1.26	0.84
11	18.3	20.0	6.67	11.7	6.67	12.7
12	8.61	5.61	4.87	1.50	4.87	2.62
13	0.95	1.90	3.17	0.95	6.35	3.17
14	3.57	1.79	3.93	3.57	5.71	1.43

Each column lists the relative error for the larger depth measurement on the calibrated imprint of Figure 6 and for a given concentration.

Table 1 Accuracy of measurements. (error %)

experiment was 0.02%. The colouring used was a blue organic dye [5].

4. Detection of the Interstices Between Teeth

4.1. Pre-processing of the 3-D Image of the Wafers

The three-dimensional images (one for each side of the wafer) are thresholded to separate the wafer from the background. Figure 7 shows a thresholded image. Interstices between adjacent teeth are detected on this type of image.

All segmentation operations on a wax wafer image use the middle axis of the imprint as a reference. The image of the wafer is scanned from the upper right to the upper left along the scanlines shown in light color in Figure 8. Points located at the midpoints between the extremities of the imprint along each scanline are detected. A cubic spline is fitted to these point. This spline curve is considered as the axis of the wax wafer. Figure 8 shows the axis as a dark solid line.

The wax wafer is often put out of shape after the bite. This deformation must be taken into account before the

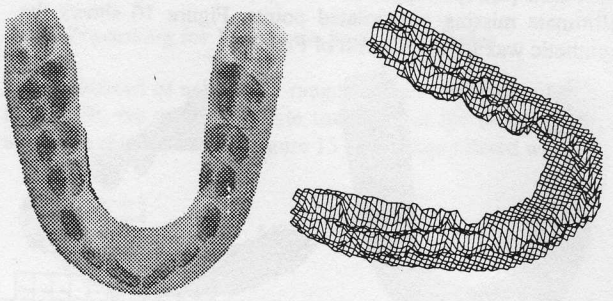

Figure 7 Thresholded dental imprint image.

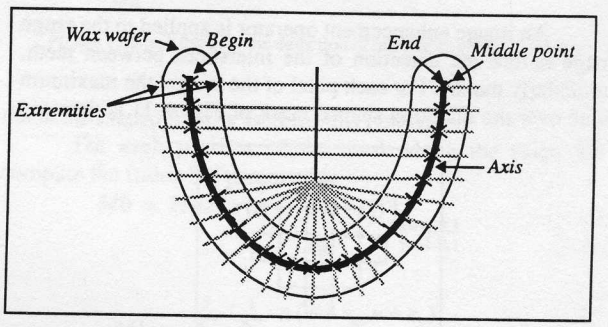

Figure 8 Wax wafer axis.

interstices between teeth are found. For this purpose, we build a synthetic wafer that follows the general shape of the wafer without the teeth imprints. The method used to build this synthetic wafer is to interpolate values linearly between the lingual and the buccal sides of the image of the imprint on a ruler with a direction perpendicular to its axis as shown in Figure 9. Then a morphological opening followed by a closing

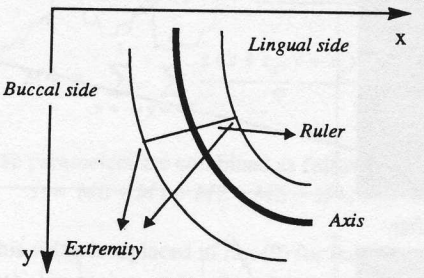

(a) Top view

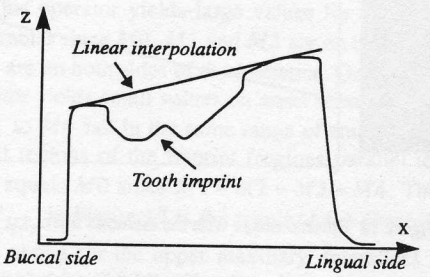

(b) Cross section

Figure 9 Synthetic wafer construction.

operation [1],[4] is applied to the synthetic wafer in order to eliminate missing interpolated points. Figure 10 shows the synthetic wax for the imprint of Figure 7.

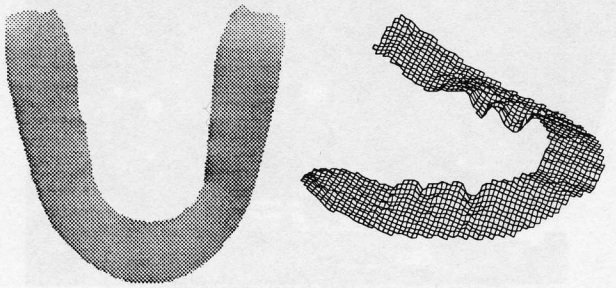

Figure 10 Synthetic wax

An image enhancement operator is applied to the range image before the detection of the interstices between teeth, particularly molars. For each pixel of the image, the maximum value over the diamond-shaped mask of Figure 11 is detected

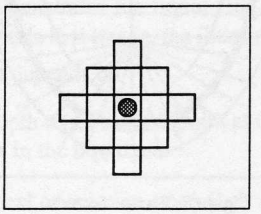

Figure 11 Diamond filter

and is assigned to the central pixel of the mask. As shown in Figure 12, this operator amplifies the interstices between teeth

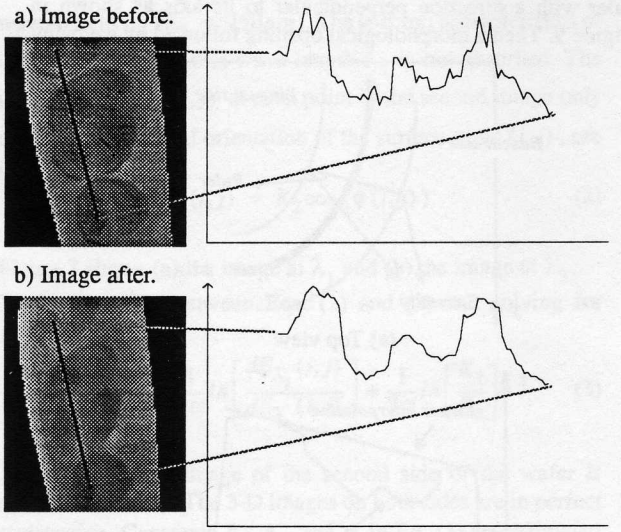

Figure 12 Filtered image with the diamond filter.

and smithies false interstices in the disto-buccal and distal fossae area [7] of molars. However, the operator has a spurious effect in the incisors area and, as demonstrated in the next section, its output will be used only in the molar area.

4.2. Separation Between Teeth

The axis drawn in Figure 8 is used to find the interstices between teeth. For each point along this axis, starting at the upper left end (s_o), we slide a ruler, oriented at different angles in the x,y plane relative to the axis. The function $\sigma(s_i)$ defined in Eq. (4) is computed for each value of s_i, the parametric distance along the axis.

$$\sigma(s_i) = \underset{j=-4,-3,-2,-1,0,1,2,3,4}{\text{Max}} [\Re(s_i, \theta_j)] \quad (4)$$

θ_j is the angle between the ruler and a perpendicular line to the axis at position s_i.

$$\theta_j = \theta_{s_i} + j\frac{\pi}{12} + \frac{\pi}{2} \qquad j=-4,-3,-2,-1,0,1,2,3,4 \quad (5)$$

θ_{s_i} is the angle of a tangent to the axis at the parametric position s_i. Figure 13 depicts the different angular definitions.

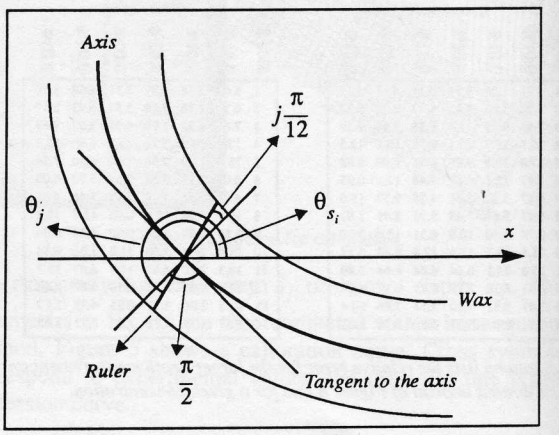

Figure 13 Angular definitions.

In Eq. (4), $\Re(s_i, \theta_j)$ is a normalized sum of values measured on the image of the imprint along the ruler for every angle. It is defined as:

$$\Re(s_i, \theta_j) = -\frac{\omega(s_i, \theta_j)}{l(s_i, \theta_j)}. \quad (6)$$

$\omega(s_i, \theta_j)$ is a weighted sum on the ruler:

$$\omega(s_i, \theta_j) = \sum_{\mu} d(s_i, \theta_j, \mu)\, w(s_i, \theta_j, \mu) \quad (7)$$

and $l(s_i, \theta_j)$ is the sum of the weights $w(s_i, \theta_j, \mu)$ on the ruler:

$$l(s_i, \theta_j) = \sum_{\mu} w(s_i, \theta_j, \mu) \quad (8)$$

$w(s_i, \theta_j, \mu)$ is a weighting factor applied to $d(s_i, \theta_j, \mu)$. μ is the parametric distance on the ruler and has the center point of

the ruler for origin. $d(s_i, \theta_j, \mu)$ is defined differently for upper maxillary incisors, molars on both maxillaries, and lower maxillary incisors. $\omega(s_i, \theta_j, \mu)$ is also defined differently for incisors and molars.

4.2.1. Processing for Upper Maxillary Incisors.

Referring to Figure 14, the wafer is divided in two parts along the ruler: the buccal side and the lingual side. z and z_r are range values measured on the buccal side of the axis, and z_2 and z_{r_2} are values measured on the lingual side of the axis. z_r and z_{r_2} are measured on the synthetic wax, and z and z_2 are measured on the actual dental imprint image. z and z_2, as z_r and z_{r_2}, have opposite location and have the same distance μ to the intersection of the axis with the ruler. Note that the range

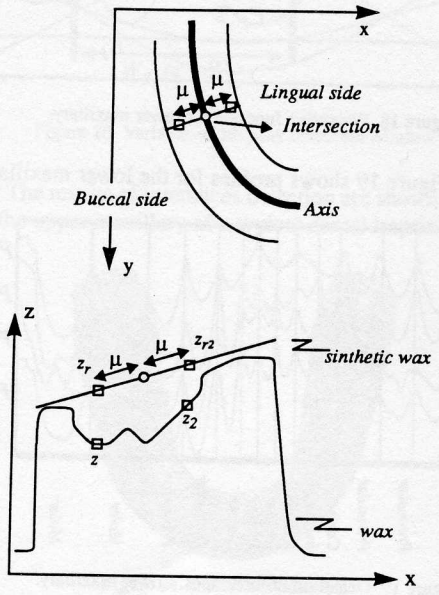

Figure 14 Mirror values.

values are measured on the 3-D image of the upper maxillary prior filtering with the diamond-shaped filter described in section 4.1.

Using values shown in Figure 14, $d(s_i, \theta_j, \mu)$ in Eq. (7) is defined as:

$$d(s_i, \theta_j, \mu) = Max[z(\mu) - z_r(\mu), z_2(\mu) - z_{r_2}(\mu)] \quad (9)$$

and $\omega(s_i, \theta_j, \mu)$ is set to $[d(s_i, \theta_j, \mu)]^2$. The curved labelled P_{IS_D} in Figure 17 is the result of the computation of the operator in Eq. (4)-(9) along the curved axis of the imprint. The operator is very reliable in the upper maxillary incisors area since large peaks appear on the curve between adjacent teeth. However, it is less performing in the molar area since peaks may appear that are not interstices between teeth but rather belong to the distal fossae or disto-buccal cusp of the molars. For this reason, a more robust operator has been defined for the detection of interstices between molars on both maxillaries.

4.2.2. Processing for Molars on both Maxillaries.

Instead of using only ranges values along the ruler, as in Eq. (9), we rather compute functions of the range values under the mask shown in Figure 15 The image filtered with the

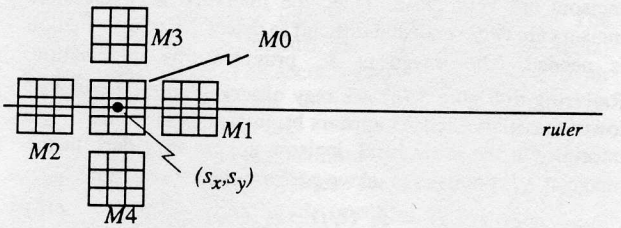

Figure 15 Mask used for the detection of interstices between molars.

diamond-shaped filter is used for this purpose.

For each position of the mask along the ruler, we compute the following parameters:

$$M0 = Max[z(x+s_x, y+s_y)]_{\substack{x=-1,0,1 \\ y=-1,0,1}} \quad (10)$$

$$M1 = \sum_{x=3}^{5} \sum_{y=-1}^{1} \frac{z(x+s_x, y+s_y)}{9} \quad (11)$$

$$M2 = \sum_{x=-5}^{-3} \sum_{y=-1}^{1} \frac{z(x+s_x, y+s_y)}{9} \quad (12)$$

$$M3 = \sum_{x=-1}^{1} \sum_{y=3}^{5} \frac{z(x+s_x, y+s_y)}{9} \quad (13)$$

$$M4 = \sum_{x=-1}^{1} \sum_{y=-5}^{-3} \frac{z(x+s_x, y+s_y)}{9} \quad (14)$$

Then, these parameters are combined as follows:

$$z = M0 + M1 + M2 - M3 - M4. \quad (15)$$

This value is replaced in Eq. (9) for the computation of $d(s_i, \theta_j, \mu)$. For molars, $\omega(s_i, \theta_j, \mu)$ is set to $d(s_i, \theta_j, \mu)$.

This operator yields large values for z on interstices between molar since $M0$, $M1$ and $M2$ are on the interstice and $M3$, $M4$ are on both sides of the interstice. On the other hand, the operator yields small values on areas occupied by a molar since $M1$ to $M4$ fall in the same range of small z values. On horizontal regions of the imprint (regions parallel to the x,y plane), z equals $M0$ since $M1 \approx M2 \approx M3 \approx M4$. The curved labeled P_{MS_F} in Figure 17 is the result of the processing step described above for the upper maxillary. Interstices between molars are clearly visible and correspond to large peaks on the curve. Peaks caused by the distal fossae and the disto-buccal cusps of molars are very small compared to those that were

visible on the P_{IS_D} curve used for upper maxillary incisors. However, peaks that correspond to interstices between incisors are not as sharp on the P_{MS_F} curve as they were on the P_{IS_D}.

4.2.3. Processing for Lower Maxillary Incisors.

Lower maxillary incisors are very small and adjacent incisors are very close. Thus, the interstice between these incisors are very small and difficult to detect. More information is needed. The image at λ_2 provides this information. Referring to Figure 3 (b), we may observe that the bottom of lower maxillary incisors appears brighter then the sides of the imprint. On the other hand, incisors appear very dark in the image at λ_1. For each pixel we perform the substraction

$$z(i,j) = z_{\lambda_1}(i,j) - z_{\lambda_2}(i,j) \qquad (16)$$

and use this resulting value in Eq. (9). Substracting the image at λ_1 from the image at λ_2 yields an output image with significantly deeper values in the incisors area. A side effect is the amplification of the interstices between adjacent incisors

4.2.4. Combination of the Operators.

The operators described above behave differently depending on the area of the imprint they are applied to. The output profiles of the operators are combined to yield a resulting profile that is used to find the interstices between teeth. For the upper maxillary the resulting profile P_S is computed as a weighted sum of the individual profiles

$$P_S = P_{IS_D} + F_S P_{IS_F} + (1 - F_S) P_{MS_F} \qquad (17)$$

where F_S is defined as:

$$F_S = \frac{1 - \cos\frac{2\pi s_i}{L}}{2} \qquad (18)$$

L is the total length of the axis of the imprint. Figure 16 shows the weighting functions F_S and $(1 - F_S)$. These weighting

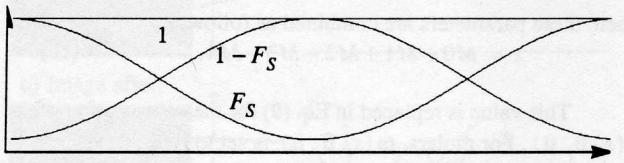

Figure 16 Weighting functions for upper maxillary.

functions increase the contribution of P_{IS_F} in the incisors area and reduces its effect in the molar area (see Figure 17). The reverse process is observed for P_{MS_F}. For the lower maxillary, the weighted sum is

$$P_I = F_I P_{II_F} + F_I P_{II_{A-I}} + (1 - F_I) P_{MI_F} \qquad (19)$$

with

$$F_I = 1 - \cos\frac{2\pi s_i}{L} \qquad (20)$$

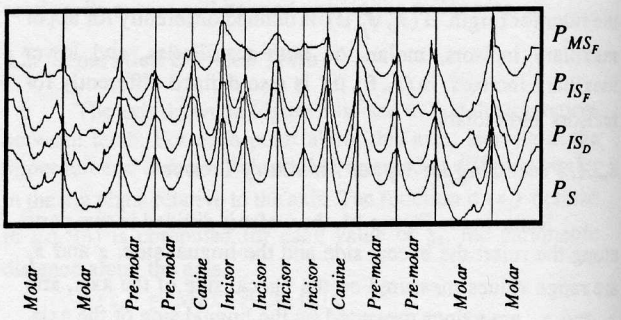

Figure 17 Detection of interstices. Upper maxillary.

Figure 18 shows the weighting function for the lower

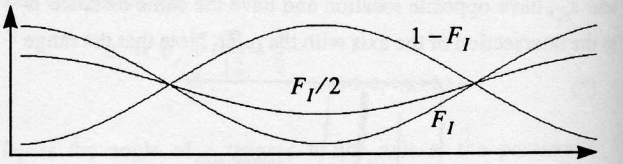

Figure 18 Weighting function for lower maxillary.

maxillary. Figure 19 shows profiles for the lower maxillary. It

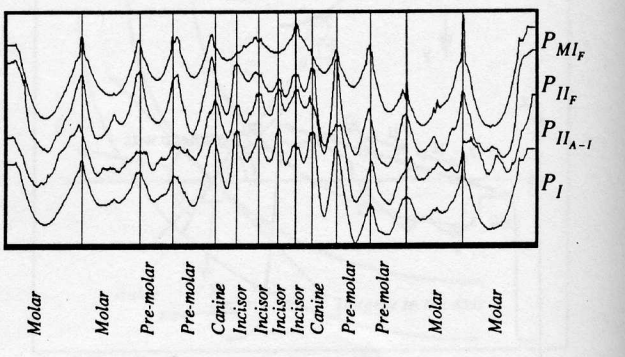

Figure 19 Detection of interstices. Lower maxillary.

is important to mention that the operators described above perform equally well for canines and pre-molars. No special operator was designed for these teeth.

4.3. Peak Detection.

From the final profiles (P_S for upper maxillary and P_I for lower maxillary), the detection of interstices between teeth is reduced to a peak detection operation. The interstices correspond to high peaks on the profiles. To eliminate small peaks we use a variable-width peak detection window. The width is set using the parametric position of the ruler along the wax of the imprint. The width for the upper maxillary (W_{S_i}) and lower maxillary (W_{I_i}) are defined as follow:

$$W_{S_i} = Max\left[\frac{L}{45}\left(1 + \cos\frac{2\pi\,(s_i - 2\frac{L}{45})}{L}\right) + \frac{L}{90}, 8\right] \qquad (21)$$

$$W_{I_i} = Max\left[\frac{L}{45}\left(1+\cos\frac{2\pi\,(s_i - 2\frac{L}{45})}{L}\right)\right] + \frac{L}{90}, 7\Bigg] \quad (22)$$

L is the length of the axis. The $1/45$ factor is the average half-width of a molar compared to the length of the axis along the wax. A threshold value $L/90$ is added because the width of the window is not allowed to take the value "zero".

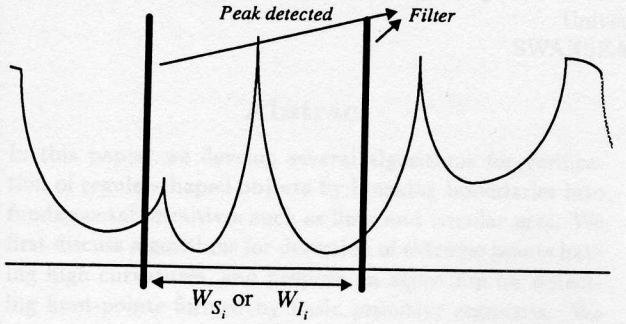

Figure 20 Variable-width peak detection window.

The results of interstices detection are shown on Figure 21 for the upper maxillary of a typical dental imprint.

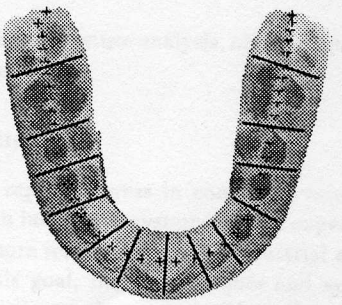

Figure 21 Interstices detected.

Small cross symbols lie on the axis and dark lines are drawn on interstices found by the algorithm.

5. Experimental Results

The image acquisition and segmentation technique described in Sections 2-4 was tested on a large number of imprints. For the experiments presented in this paper, the wax dental imprints of 13 normal subjects were recorded. The image of 15 upper maxillaries and 14 lower maxillaries were acquired with the special purpose 3-D camera (one lower maxillary imprint was rejected because of the poor quality of the imprint on the wax wafer). The 29 profiles were processed with the algorithm for interstice detection and position estimation on the 3-D image of the imprints. The algorithm correctly detected all interstices on all 29 3-D profiles. All interstices were correctly located on the axis of each imprint. The segmentation algorithm worked very well on lower maxillary incisors even with poor imprint quality. Furthermore, the algorithm did not generate any false interstice in the disto-buccal cusp or buccal fossae of molars.

6. Conclusion

This paper has presented a computer vision system for the acquisition and the segmentation of 3-D profiles of wax dental imprints. The system is part of an expert system for automatic orthodontic diagnosis. The acquisition system is based on the absorption of light by a dispersive medium. The 3-D profiles of wax imprints measured with this special purpose camera showed an accuracy better than 10% for depth measurements, and better than 5% for lateral distance measurements on the imprint.

The segmentation algorithm searches for the interstices between teeth on both maxillaries. The algorithm is based on three different operators, each operator being tuned for a specific type of tooth. The algorithm was tested on many 3-D profiles and all interstices were correctly detected. No false interstices were produced by the operators.

The next step on the development of the system will focus on the processing of profiles with missing teeth and on profiles with mixed dentition. A heuristic algorithm is currently under development for the identification of missing or false interstices that may appear on poorly recorded wax imprints. Tests on a larger number of imprints (>100) will also be performed. Finally, a set of 10 orthodontic parameters will be measured on the 3-D profiles and fed to the expert system for automatic diagnosis.

7. Acknowledgments

The research work was supported by Grant OGPIN 011 of the Natural Sciences and Engineering Research Council of Canada (NSERC). J. Côté was supported by a NSERC graduate scholarship. The authors would like to thank R. Houde for his help in the design of the 3-D acquisition system, L. Guimond for comments on the segmentation technique, and MM. J. Lévesque and Y. Chalifour for their work on the experimental setup.

8. References

[1] Colin C. Archibald, Stanley R. Sternberg, Mathematical Morphology Applicated to Range Image Processing. Machine Vision International Ltd., 280 Albert St., Ottawa, Canada. K1P 5G8.

[2] C. Bernard, J.M. Brodeur, A. Fournier, D. Poussart, D. Laurendeau, R. Guay, M. Olivier, and P. Retrouvey, Computerized Diagnosis in Orthodontics for Epidemiological Studies: A Progress Report, Proc. of the 66th General Session of the International Association for Dental Research, Montréal, P.Q., Canada, March 9-13, 1988, pp.169.

[3] L. Guimond, Acquisition et segmentation d'images d'empreintes dentaires, Master's thesis, Laval University, Québec, Canada, (in French).

[4] Robert M. Haralick, Stanley R. Sternberg and Xinhua Zhuang, Image Analysis Using Mathematical Morphology. IEEE Transaction on Pattern Analysis and Machine Intelligence, Vol. PAMI-9, #4, July 1987.

[5] R.Houde, D.Laurendeau and D.Poussart, 3-D camera based on differential optical absorbance, Proc. SPIE, International Symposium on Optical & Optoelectronic Applied Science & Engineering. San Diego, Cal. july 1990 (under press).

[6] D.Laurendeau, L.Guimond and D.Poussart, A Computer-Vision Technique for the Acquisition of 3D Profiles of Dental Imprints and the Detection of Teeth in the Profiles: An Application in Orthodontics, to appear in IEEE Transaction on Medical Imaging.

[7] J.H. Scott and N.B.B. Symons, Introduction to Dental Anatomy. 9th Edition, Churchil Livingstone, New York 1982.

[8] John W.T. Walsh, Photometry. Constable, London 3d edition 1958.